

## Hurricane Directional Wave Spectrum Spatial Variation in the Open Ocean

C. W. WRIGHT, E. J. WALSH,\* D. VANDEMARK, AND W. B. KRABILL

*NASA Goddard Space Flight Center, Wallops Flight Facility, Wallops Island, Virginia*

A. W. GARCIA

*U.S. Army Engineer Research and Development Center, Vicksburg, Mississippi*

S. H. HOUSTON,+ M. D. POWELL, P. G. BLACK, AND F. D. MARKS

*Hurricane Research Division, NOAA/AOML, Miami, Florida*

(Manuscript received 28 August 2000, in final form 1 March 2001)

### ABSTRACT

The sea surface directional wave spectrum was measured for the first time in all quadrants of a hurricane's inner core over open water. The NASA airborne scanning radar altimeter (SRA) carried aboard one of the NOAA WP-3D hurricane research aircraft at 1.5-km height acquired the open-ocean data on 24 August 1998 when Bonnie, a large hurricane with 1-min sustained surface winds of nearly  $50 \text{ m s}^{-1}$ , was about 400 km east of Abaco Island, Bahamas. The NOAA aircraft spent more than five hours within 180 km of the eye and made five eye penetrations. Grayscale coded images of Hurricane Bonnie wave topography include individual waves as high as 19 m peak to trough. The dominant waves generally propagated at significant angles to the downwind direction. At some positions, three different wave fields of comparable energy crossed each other. Partitioning the SRA directional wave spectra enabled determination of the characteristics of the various components of the hurricane wave field and mapping of their spatial variation. A simple model was developed to predict the dominant wave propagation direction.

### 1. Introduction

The NASA/Goddard Space Flight Center/Laboratory for Hydrospheric Processes and the NOAA/Atlantic Oceanographic and Meteorological Laboratory/Hurricane Research Division (HRD) combined their resources to provide the first documentation of the sea surface directional wave spectrum in all quadrants of a hurricane in open water. On 24 August 1998, one of the NOAA/Aircraft Operations Center (AOC) WP-3D hurricane research aircraft, N43RF, carried the NASA scanning radar altimeter (SRA) into Hurricane Bonnie. At the time, Bonnie was a Saffir–Simpson scale (Saffir 1977; Simpson and Reihl 1981) Category 3 hurricane according to Avila (1998).

Figure 1 shows the Hurricane Bonnie track with the

filled circles indicating the eye positions observed by either the NOAA aircraft or the U.S. Air Force Reserve hurricane hunter aircraft while the SRA was in the vicinity of Bonnie. The track of Bonnie was  $315^\circ$  for about 4 h before the NOAA aircraft arrived and for 4 h after it departed, but it deviated northward during the observation period.

The SRA (Walsh et al. 1996) and its predecessor, the Surface Contour Radar (Walsh et al. 1985, 1989), were designed primarily to measure the energetic portion of the directional wave spectrum by generating a topographic map of the sea surface. The SRA general measurement geometry is shown in Fig. 2; the specific numbers refer to the Hurricane Bonnie flight on 24 August 1998.

The SRA sweeps a radar beam of  $1^\circ$  (two way) half-power width across the aircraft ground track over a swath equal to 0.8 of the aircraft height, simultaneously measuring the backscattered power at its 36-GHz (8.3 mm) operating frequency and the range to the sea surface at 64 positions. The scan rate was 8 Hz during the Bonnie flight. (It is presently 10 Hz, but faster scan rates are possible.) In real time, the slant ranges are multiplied by the cosine of the off-nadir incidence angles (including the effect of aircraft roll attitude) to determine the

\* Currently on assignment: NOAA Environmental Technology Laboratory, Boulder, Colorado.

+ Current affiliation: National Weather Service Forecast Office, CPHC/NOAA, Honolulu, Hawaii.

Corresponding author address: C. Wayne Wright, Code 972, NASA Goddard Space Flight Center, Wallops Flight Facility, Wallops Island, VA 23337.

E-mail: wright@osb.wff.nasa.gov

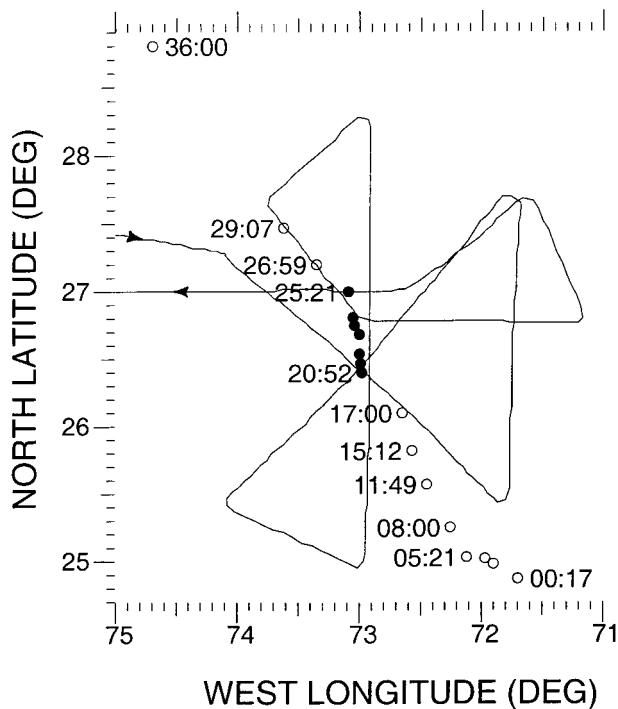


FIG. 1. Eye positions of Hurricane Bonnie observed by the NOAA research aircraft or the U.S. Air Force Reserve hurricane hunter aircraft. The filled circles indicate the eye positions observed during the SRA data-collection interval. The observation times beside the eye locations are UTC on 24 Aug 1998, with 24 h added to the observation times on 25 Aug. The NOAA aircraft ground track is shown, except that two loops it made at 27.3°N, 74.1°W and 26.35°N, 73.1°W have been deleted so they would not be mistaken for eye locations.

vertical distances from the aircraft to the sea surface. These distances are subtracted from the aircraft height to produce a sea-surface elevation map, which is displayed on a monitor in the aircraft to enable real-time assessments of data quality and wave properties.

Because the SRA directional wave spectra are represented in terms of ocean wave propagation vectors in wavenumber space, the wind is referenced to the direction toward which it is blowing, rather than the meteorological convention, to make it easier to assess differences in the wind and wave directions on the plots.

Observation-based surface wind analyses for hurricanes are produced routinely by HRD (Powell et al. 1996). These wind fields are provided in real time for operational use by forecasters at the National Hurricane Center. A real-time storm-centered analysis was performed at HRD for Hurricane Bonnie at 0130 UTC 25 August 1998, which incorporated the NOAA flight-level winds adjusted to 10-m height above the surface, some Cooperative Institute for Meteorological Satellite Studies geostationary low-level visible satellite cloud-tracked winds adjusted to the surface (Dunion et al. 2001, manuscript submitted to *Mon. Wea. Rev.*), and a few ship and buoy reports. The surface wind vectors

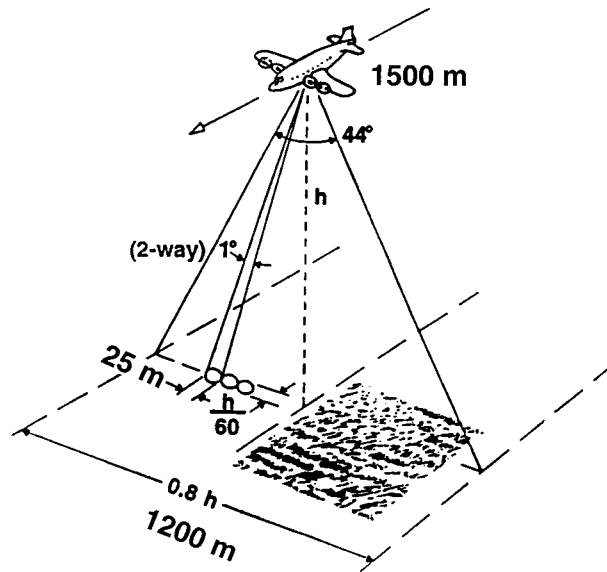


FIG. 2. Measurement geometry of the SRA. The specific numbers refer to the Hurricane Bonnie flight on 24 Aug 1998.

used throughout this paper were extracted from that surface wind analysis.

## 2. Wave topography

Figure 3 shows three examples of SRA wave topography maps using the same grayscale coding (dark troughs and light crests). The time sequence of the data progresses upward for the three 8-km segments, independent of the actual flight-line orientation. At the flight level of 1.5 km, the SRA swath width was 1.2 km and the images are in proportion. The topography for the left-hand image was obtained while the aircraft was traveling northward about 150 km north of Hurricane Bonnie's eye. The waves were predominantly swell propagating toward 330°, and the periodic oscillation in the height of the waves associated with the narrow spectral width is apparent in the image. The significant wave height ( $H_s$ , 4 times rms surface elevation) was about 10 m, and the dominant wavelength was about 300 m.

The HRD surface wind at this location was directed toward the west at about  $40 \text{ m s}^{-1}$ . A secondary, shorter wavelength system generated by this wind can be seen propagating from right to left across the image, which was parallel to the wind direction.

The wave topography in the middle image of Fig. 3 was obtained while the aircraft was traveling south-eastward about 30 km south and 40 km east of the eye. Here  $H_s$  was over 6 m, and the wave field was bimodal with approximately the same energy in the two components. The sea surface topography for the image on the right was acquired traveling northward about 120 km east and 90 km south of the eye, where  $H_s$  was over 7 m and the wave field was trimodal.

To emphasize that the images of Fig. 3 represent wave

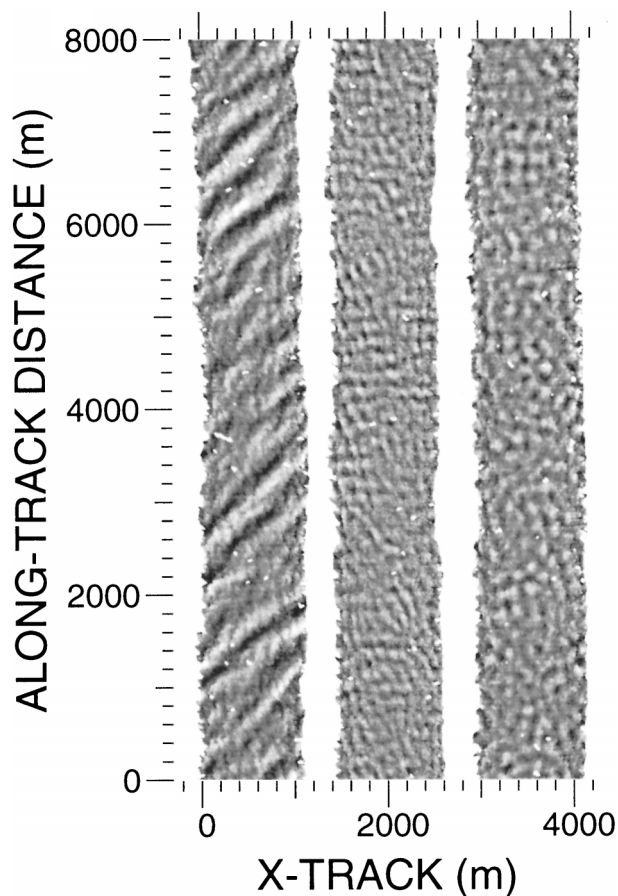


FIG. 3. Wave topography maps produced by the SRA displayed with the same grayscale coding (dark troughs and light crests). The isolated white speckles and the white line at 3700 m alongtrack and 200 m cross-track are data dropouts. The left-hand and middle images involve about 550 crosstrack scan lines acquired over 71 s. The right-hand image involves only about 400 scan lines acquired over 51 s because the aircraft ground speed was faster.

topography, Fig. 4 shows the surface elevation profiles from cross-track positions 30 and 37 (of 64 starting from the left-hand side of the SRA swath) for the interval between 5 and 8 km on the left-hand image in Fig. 3. Cross-track position 30 goes through the highest position on the crest of the large wave, 11 m above sea level. It misses the deepest part of the trough, which is lined up directly behind the highest part of the crest in the direction of wave propagation. Cross-track position 37, which is about 100 m to the right of position 30, profiles the deepest part of the trough, which is 8 m below sea level. The crest-to-trough height was 19 m with a 178-m separation, which corresponds to a 356-m wavelength.

Figure 5 shows contours of the smoothed  $H_s$  spatial variation measured by the SRA during the 5 h it was in the vicinity of Hurricane Bonnie on 24 August 1998. The smallest waves are in the vicinity of the radius of maximum wind in the southwest quadrant, and the largest waves are in a similar position in the northeast quad-

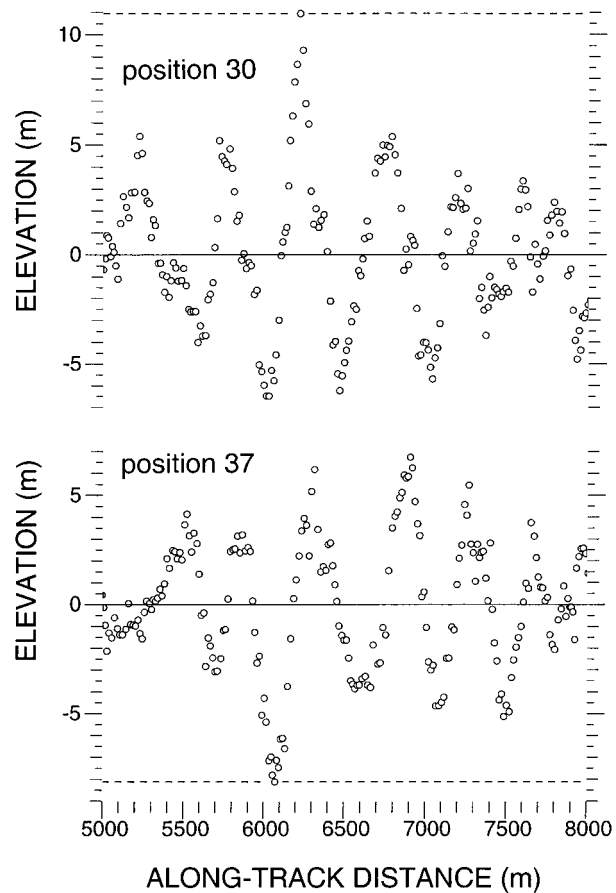


FIG. 4. Surface elevation profile from cross-track positions 30 and 37 (of 64 starting from the left-hand side of the SRA swath) for the interval between 5 and 8 km on the left-hand image in Fig. 3.

rant. While accurate and valuable, Fig. 5 should be considered a simple characterization of the wave field whose complexities are evident in Fig. 3.

### 3. Directional wave spectra

The sea-surface topography measured by the SRA is interpolated to a uniform grid and transformed by a two-dimensional FFT. The artifact spectral lobes are deleted, and the real lobes are Doppler corrected. The appendix describes these processes in detail.

Figures 6–9 show wavenumber directional wave spectra generated from SRA topography measured in Hurricane Bonnie on 24 August 1998. The time sequence progresses from left to right and top to bottom. The map in the upper left-hand panel superimposes the storm-centered track of the NOAA aircraft on the HRD surface wind field. The wind radials extend downwind. This is opposite to the convention used in meteorology, but it is useful for comparison with the wave spectra presented here. A speed of  $30 \text{ m s}^{-1}$  corresponds to a length of 10 km. The spacing between adjacent wind vector locations is 20 km. The circles on the map show

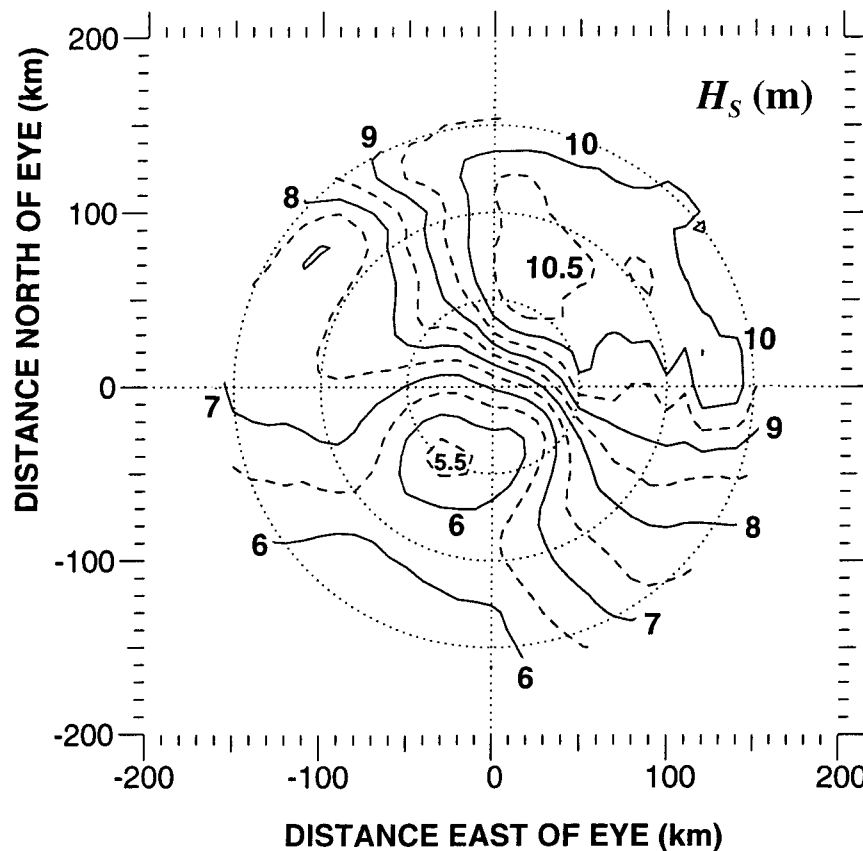


FIG. 5. Spatial variation in  $H_s$  measured by the SRA in Hurricane Bonnie on 24 Aug 1998. Contours for integer values of wave height (in meters) are solid and contours for integer values plus 0.5 m are dashed.

the locations of the 15 spectra with the circle corresponding to the first spectrum in the sequence filled.

The SRA spectral observations presented in this paper spanned from 2030 UTC 24 August to 0144 UTC 25 August. The 60 spectra in Figs. 6–9 have been selected to show the significant features of the wave-field spatial variation and provide detailed information on the spectral shapes.

The spectra are in a north, east ( $k_n$ ,  $k_e$ ) linear wave-number coordinate system with direction being toward which the waves are propagating. Each spectrum contains nine contours, linearly spaced from 10% to 90% of the peak spectral density of that spectrum, which in  $(\text{rad m}^{-1})^2$  equals the number in the lower right-hand corner times 81 342. The half-power contour is thicker.

The thick radials in Figs. 6–9 indicate the orientations of the boundaries of the half-planes used to eliminate the spectral artifact lobes. To be able to deal with complex situations (such as real spectral lobes in opposite half-planes), there are separate boundaries for wavelengths less than 150 m and greater than 150 m, although they frequently have the same orientation. All spectral energy is deleted on the artifact side of the boundary,

but subsequent Doppler corrections sometimes push the contours past the boundaries.

Two dashed radials are used to partition each spectrum into one to three components. The three pairs of numbers separated by a slash in the header of each spectrum are the wave height (in meters, equal to four times the square root of the spectral variance within the partition) and the dominant wavelength (in meters, determined from  $k_n$  and  $k_e$  at the highest spectral value within the partition). The sequence of the three sets of numbers is in clockwise (CW) order around the spectrum. When only two wave components are identified, the two dashed radials are placed coincident between them, so the middle elements in the header are zero. When only one component is identified, the two dashed radials are placed coincident at one of the half-plane boundaries, but, in this case, some spurious numbers still show up in the third header entry.

The location north and east of the eye (in kilometers) is indicated in the upper left-hand corner of each spectrum. The total  $H_s$  is shown in the upper right-hand corner. In the lower left-hand corner are the flight segment (1–10) and spectrum number, separated by a hy-

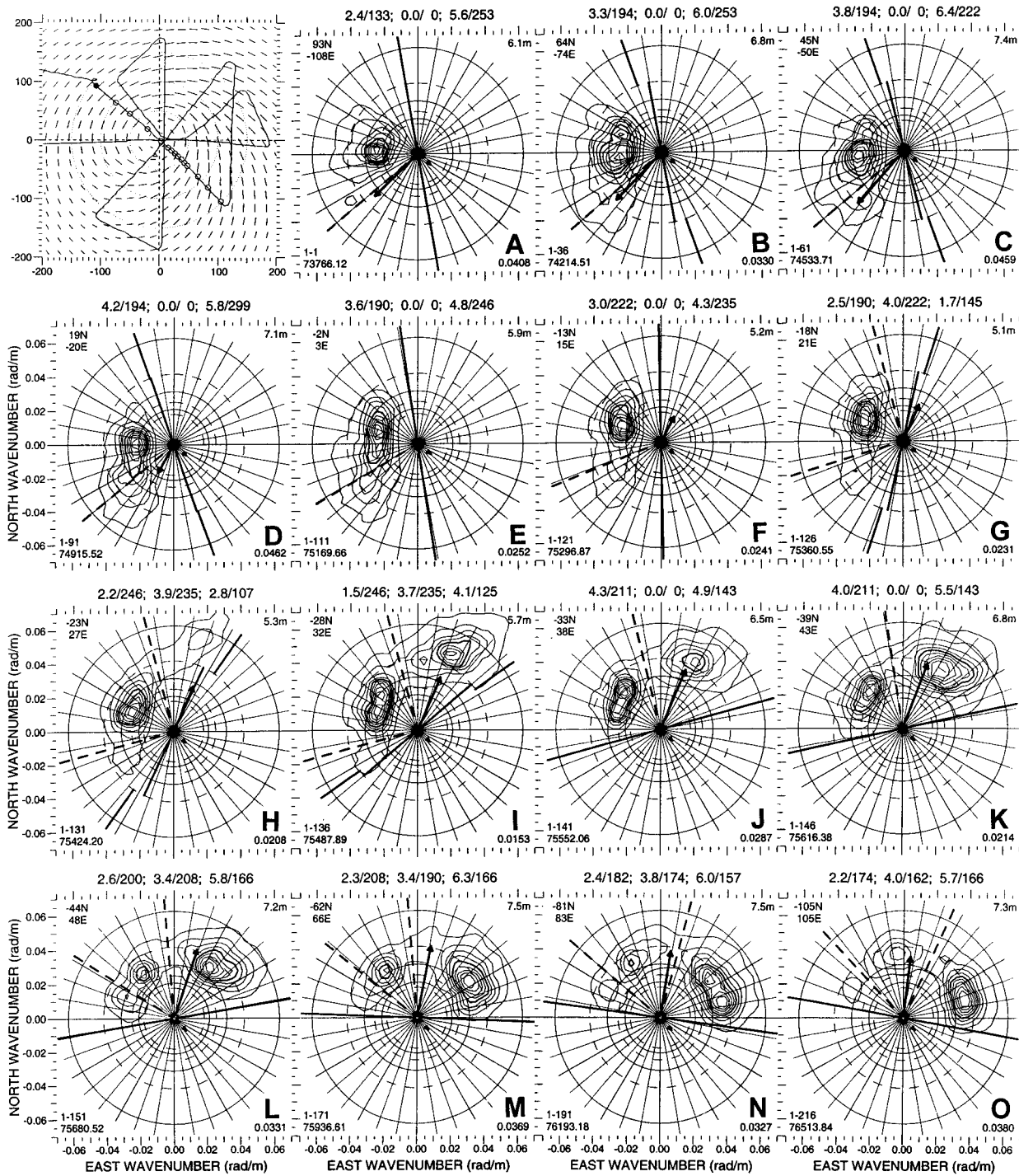


FIG. 6. SRA directional wave spectra acquired between 2030 and 2115 UTC 24 Aug 1998. The map in the upper left-hand panel superimposes the NOAA aircraft track on the HRD surface wind field with radials extending downwind. A speed of  $30 \text{ m s}^{-1}$  corresponds to a length of 10 km. The 15 circles indicate the locations of the 15 spectra, and the circle corresponding to the first spectrum in the sequence is filled. Wave direction is toward that in which the waves are propagating.

phen, and the second of the day (with 86 400 added after midnight).

The outer solid circle on each spectrum indicates a wavelength of 100 m, and the inner circles correspond

to wavelengths of 200 and 300 m. The three dashed circles correspond to wavelengths of 150, 250, and 350 m.

The arrow superimposed on each spectrum points in

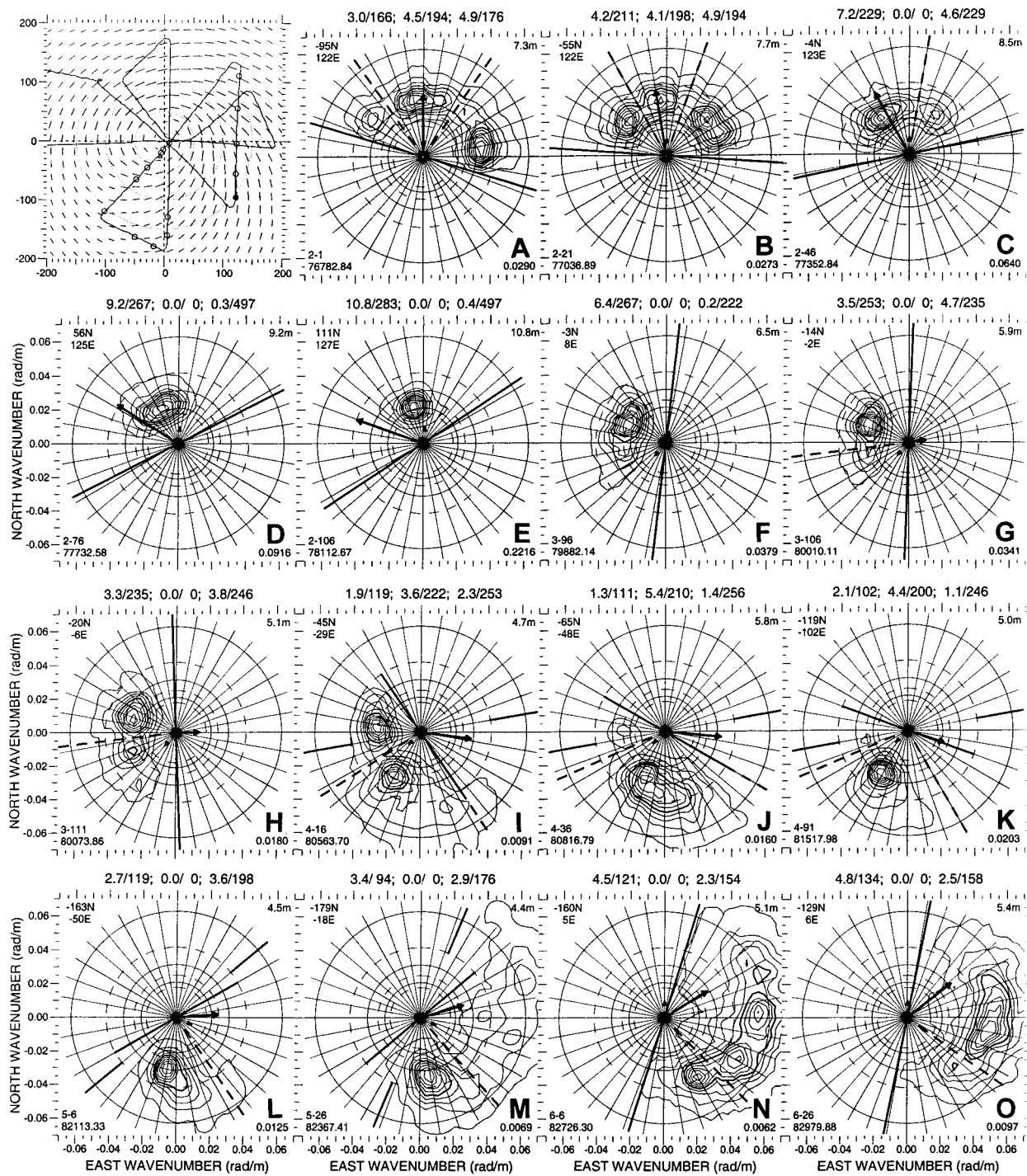


FIG. 7. SRA directional wave spectra acquired between 2120 and 2303 UTC 24 Aug 1998 in the same format as Fig. 6.

the downwind direction given by the HRD surface wind field. The wind speed values were divided by 1000 before plotting, so a speed of  $40 \text{ m s}^{-1}$  corresponds to a length of  $0.04 \text{ rad m}^{-1}$  [or approximately the 150 m wavelength circle (dashed)]. The arrow head at a distance  $0.01 \text{ rad m}^{-1}$  from the origin always points in the aircraft flight direction.

At the start of the flight pattern (Fig. 6a), the dominant wave system was a swell of  $5.6 \text{ m } H_s$  and  $253 \text{ m}$  wavelength propagating toward  $275^\circ$ , even though the wind was blowing toward  $227^\circ$  at  $35 \text{ m s}^{-1}$ . This deviation of the dominant wave direction on the order of  $40^\circ\text{--}50^\circ$  CW from the local wind is a common occurrence, and it is reasonable, considering the curvature in the wind

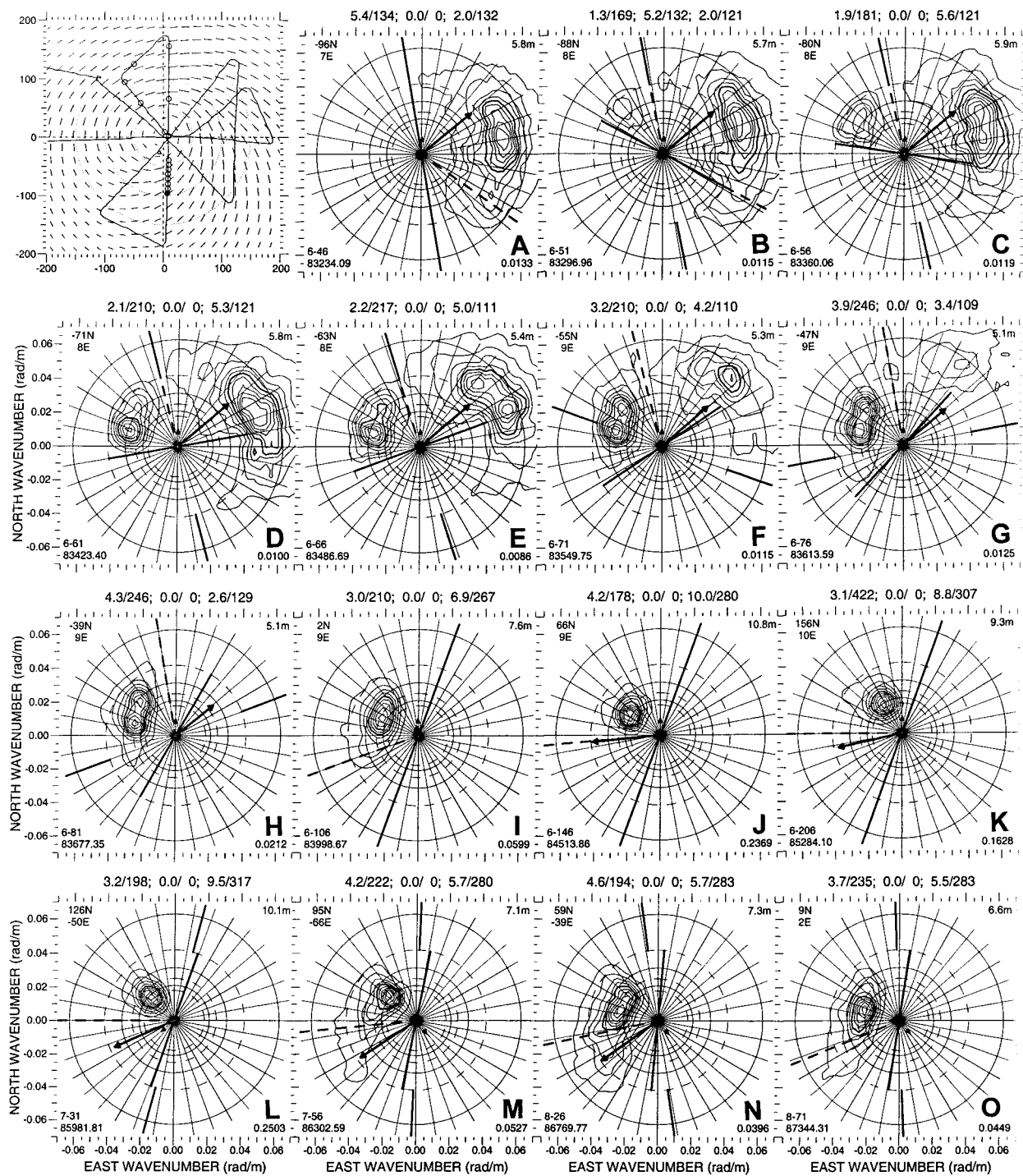


FIG. 8. SRA directional wave spectra acquired between 2307 UTC 24 Aug and 0016 UTC 25 Aug 1998 in the same format as Fig. 6.

field. The dashed partition radials are both oriented at  $230^\circ$ . Even though no contours extend into the southern partition, the energy it contains corresponds to a wave height of 2.4 m, and the wavelength at the spectral peak was 133 m. It was decided not to use log instead of linear contours to extend below the 10% level because

it made many of the spectra busy and difficult to interpret.

In Figs. 6b–d the wind-driven waves appear as a tail on the westward propagating swell, extending toward shorter wavelengths. This points up a limitation of the partitioning scheme used here. When the swell and

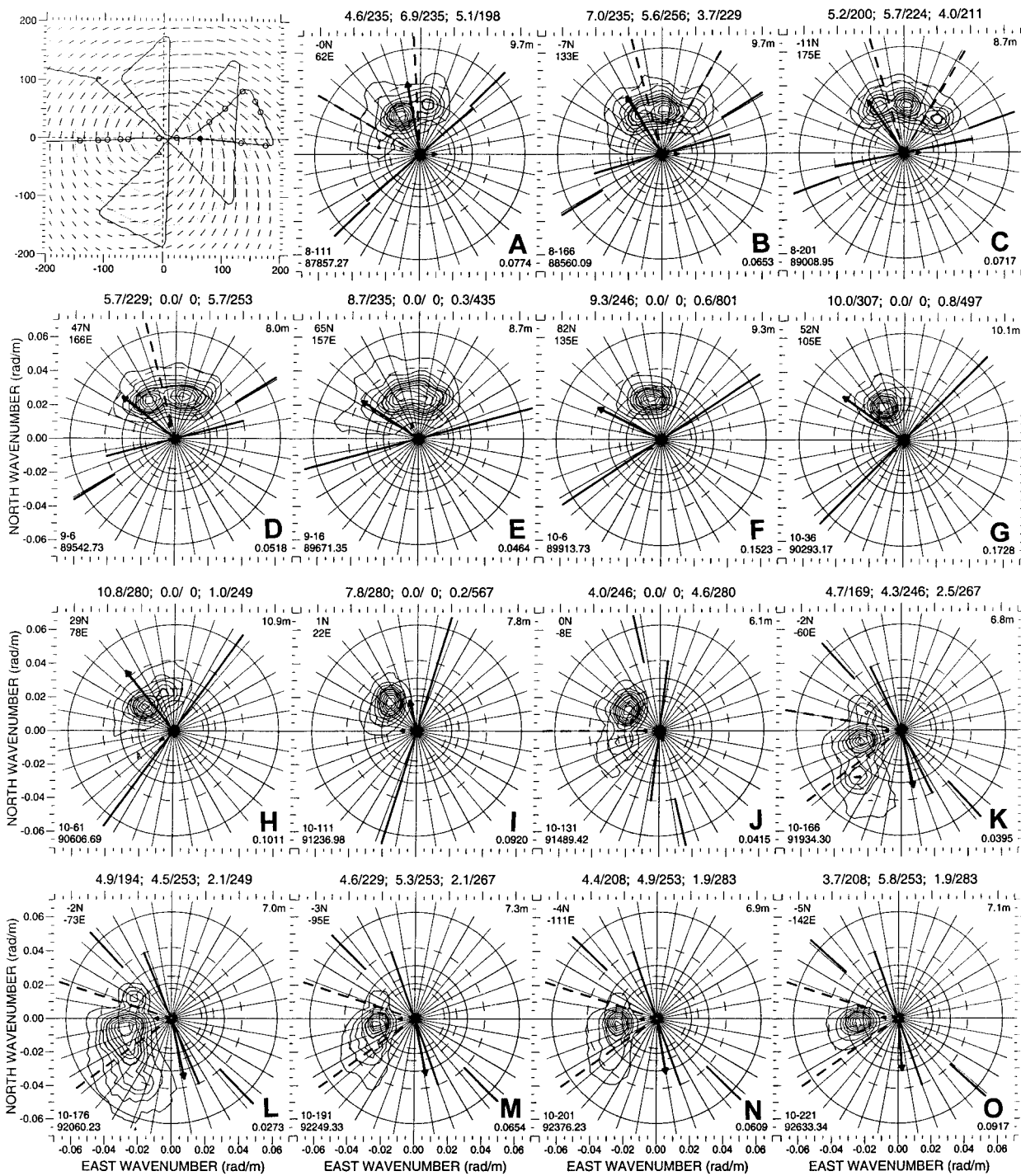


FIG. 9. SRA directional wave spectra acquired between 0024 and 0144 UTC 25 Aug 1998 in the same format as Fig. 6.

wind-driven wave components are not disjointed, the “windsea” wavelength and direction of propagation will sometimes be determined at the partition boundary when the spectral density is highest there.

Since even this simple scheme required four angles to be determined for each spectrum (two for the half-planes, two for the partitions), a more complex parti-

tioning was considered too burdensome for the present analysis. The numbers in the headers should be used with caution, but they can provide quantitative information on the wave-field components.

The spectrum shown in Fig. 6e was near the eye, and the situation was not very different from that shown in Fig. 6d except that the wind was almost zero. The se-

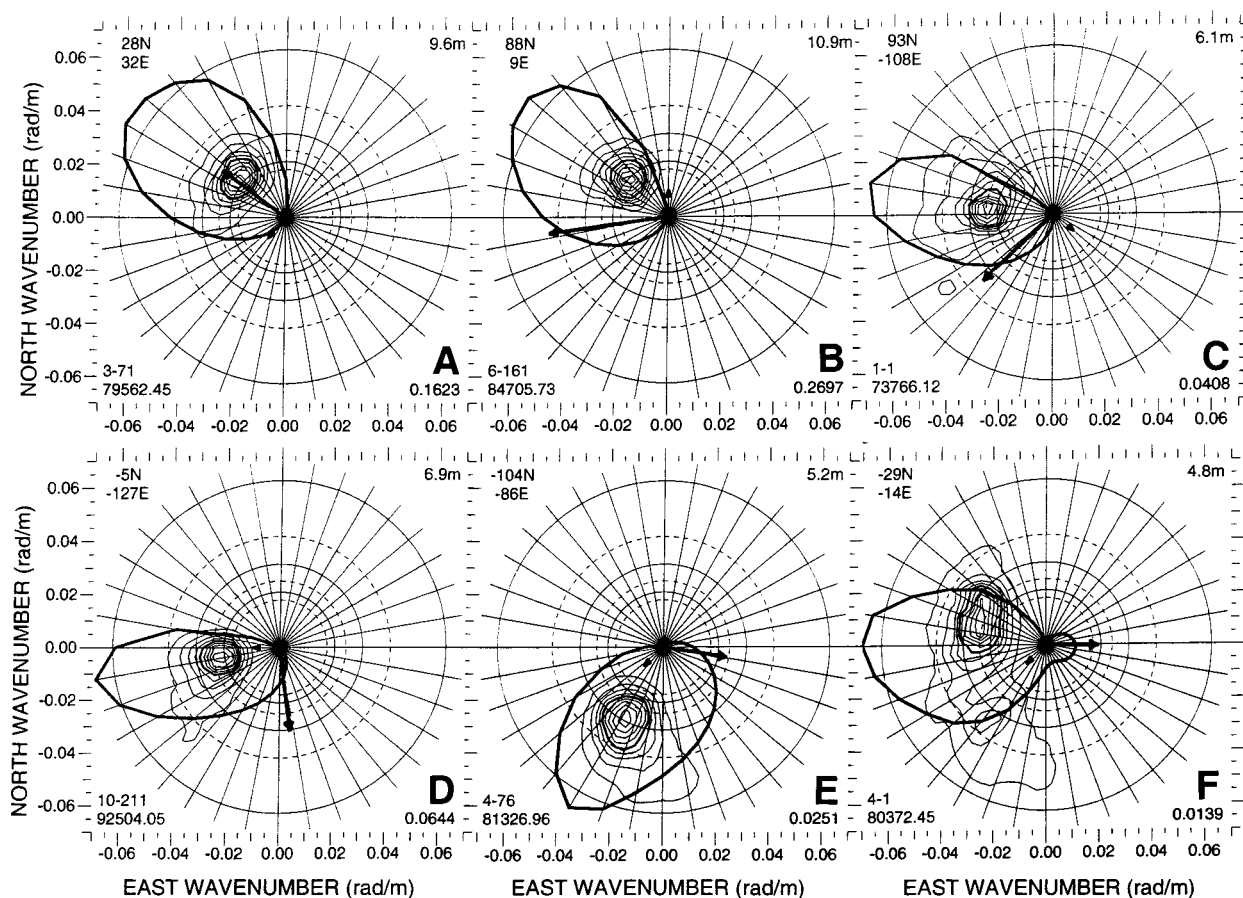


FIG. 10. Wind-weighting patterns overlaid on six spectra from various parts of Hurricane Bonnie.

quence in Figs. 6f–l shows spectra from contiguous 8-km data spans approaching the radius of maximum wind. The spectra in Figs. 6h–l show the wind-driven component growing with increasing wind from 2.8 m  $H_s$  and 107 m wavelength to 5.8 m  $H_s$  and 166 m wavelength. The swell component maintained about 4 m  $H_s$  during this sequence. As the end of the Fig. 6 flight segment was approached, the northwestward propagating swell bifurcated, and the wave field as a whole rotated CW as the wind rotated counterclockwise (CCW).

The aircraft turned northward when it was about 120 km east and 100 km south of the eye. Fifty kilometers south of the eye the wave field became strongly trimodal (Fig. 7b), with each of the three components having about 200 m wavelength and over 4 m  $H_s$ . The spectral peaks were spread over  $100^\circ$  and the span of the half-power spectral width was about  $145^\circ$ . This would likely be a particularly dangerous location for a boat, since the total  $H_s$  was 7.7 m and it was not possible to keep the bow pointed into the approaching waves.

Due east of the eye, the north and northwest wave components had coalesced (Fig. 7c), and by 56 km north of the eye (and 125 km east) only a broad northwestward propagating swell of 9.2 m  $H_s$  remained (Fig. 7d). The swell spectrum narrowed and rotated CW as the distance

north of the eye increased (Fig. 7e). The  $H_s$  increased along this flight segment from about 7 m to more than 10 m.

As the aircraft proceeded back to the eye, the swell system rotated CCW. About 40 km northeast of the eye, a CCW extrusion of the spectrum toward shorter wavelengths began that became pronounced in the eye (Figs. 7f,g). By 20 km south of the eye (Fig. 7h) the two wave fields were comparable and opposed to the local wind. Between 80 and 160 km southwest of the eye (Figs. 7j,k) the dominant waves propagated at right angles to the  $35\text{--}25\text{ m s}^{-1}$  local wind.

At 160 km due south of the eye (Fig. 7n), the wave field was quite broad with highly correlated trends in spectral density, wavelength, and propagation direction. The longest waves propagated toward the southeast, and the shortest toward the northeast. Proceeding north, the broad eastward propagating wave field consolidated and rotated CCW without much increase in  $H_s$  (Figs. 7o, 8a).

Between 96 and 39 km south of the eye (Figs. 8a–h), the wave-field composition changed radically with only a small decrease in  $H_s$ . A northwestward propagating swell appeared and increased to 4.3 m  $H_s$  and 246 m wavelength as it rotated CCW. During the same

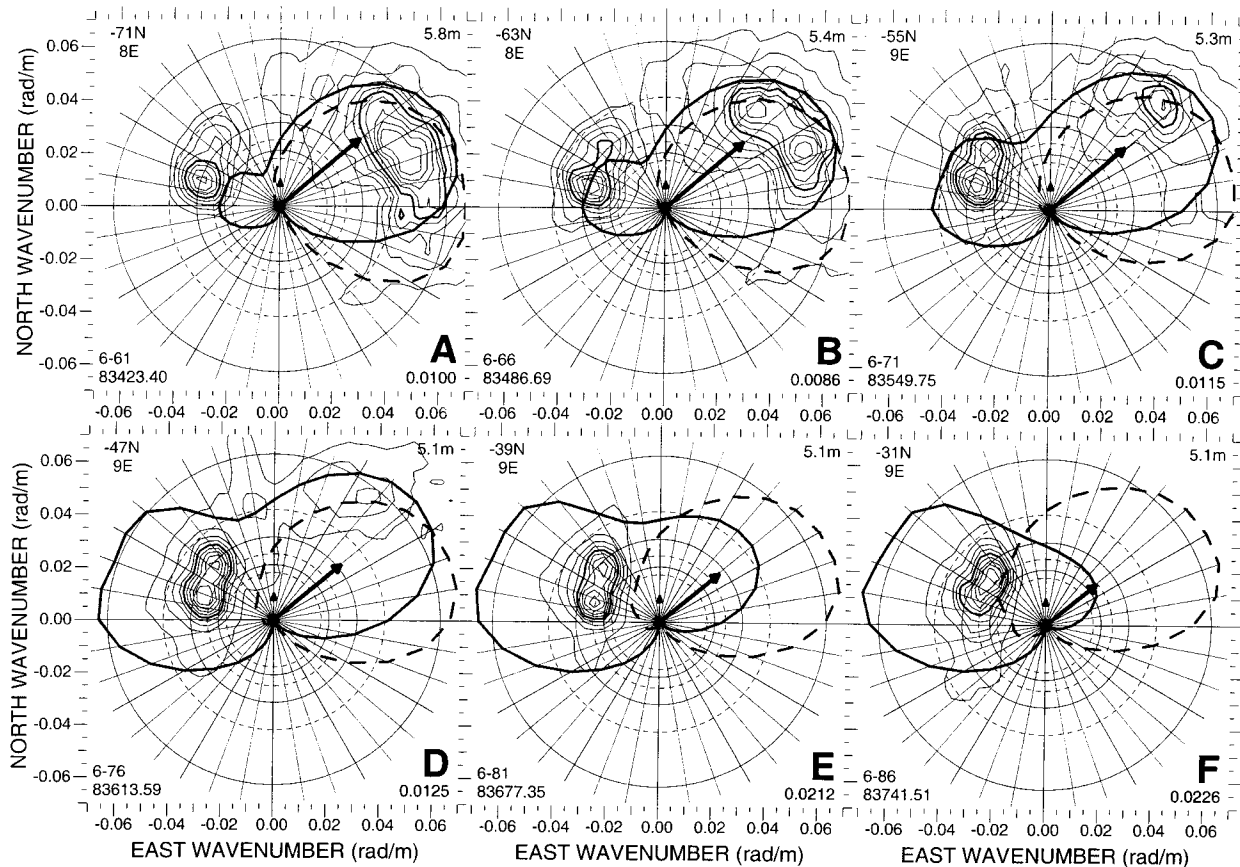


FIG. 11. Wind-weighting patterns overlaid on six spectra from one 40-km flight segment in Hurricane Bonnie. The solid patterns consider the hurricane motion over the 10 h prior to the observations, and the dashed patterns held the wind field fixed to that at the observation times.

interval, the eastward propagating system diminished from 5.8 to 2.6 m  $H_s$  as it also rotated CCW.

The spectrum had essentially the same shape between the eye (Fig. 8i) and 40 km north of the eye, but  $H_s$  increased from 7 to 10 m. At 66 km north of the eye (Fig. 8j), the spectrum was quite narrow and it rotated CW as the distance from the eye increased (Fig. 8k).

The header indicates that the swell system in the spectrum shown in Fig. 8k had 8.8 m  $H_s$  and 307 m dominant wavelength. The secondary wave system seen propagating toward the west in the left-hand image of Fig. 3 is not apparent in the spectrum (Fig. 8k) because its peak energy density was less than 10% of the swell peak. Even though the energy density for the wind-driven sea was below the lowest contour in the spectrum shown in Fig. 8k, the numbers in the header indicate that  $H_s$  associated with the wind direction was 3.1 m. The windsea spectrum would have been much broader than the narrow swell spectrum. The wind-driven wave height was probably higher since the partition boundary was only  $12^\circ$  CW of the wind vector, but, for simplicity, the partitioning process was restricted to two radials for boundaries. The 422 m dominant wavelength for the wind-driven sea partition suggests that there was some

unseen noise contamination near the origin that was higher than the wind-driven sea peak.

Figure 9 is included for completeness so that the details of the spectral shapes and spatial variations can be compared with those of the other flight lines. All the significant variations in spectral shape are displayed in Figs. 6–9. They can be used in interpreting the plan views of the spatial variation of the wave-field components discussed later in this paper.

#### 4. A simple model for predicting wave dominance

When the dominant waves were observed propagating orthogonal to a  $30 \text{ m s}^{-1}$  local wind, a simple model was developed to check on the reasonableness of the observed spectra. To study differential wave growth in Lake St. Clair, Donelan et al. (1992) used the root-mean-square (rms) wind along the propagation path rather than a linear average because wave energy scales roughly with the square of wind speed (Hasselmann et al. 1973). This analysis uses a modification of that approach.

The goal was to develop a function that would suggest the direction toward which the dominant waves would propagate at each location where a directional wave

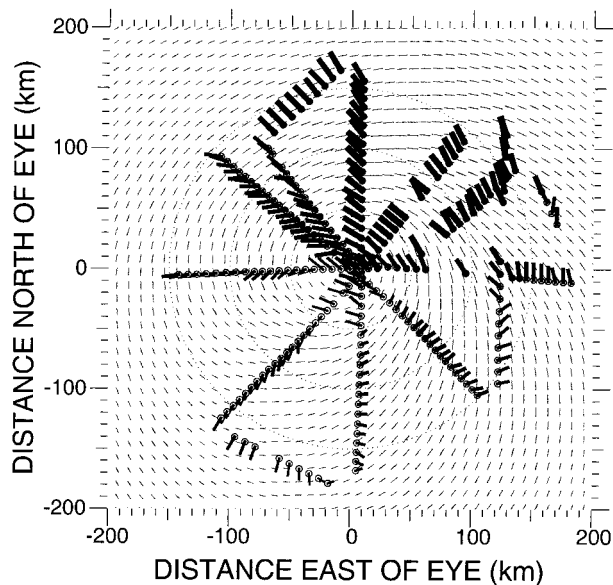


FIG. 12. Hurricane Bonnie primary wave field. The circles indicate the data locations and the radials extend in the wave propagation direction a length proportional to the wavelength. The width of the radials is proportional to the  $H_s$ , so the aspect ratio is an indication of wave steepness. The short, narrow lines indicate the HRD surface wind analysis.

spectrum was determined. At each location, for every  $10^\circ$  azimuth, the wind effect over a 300-km fetch was summed in 10-km increments. At the 31 positions along each radial direction, the wind vector from the HRD surface wind analysis was used to determine  $\phi$ , the angle between it and the radial direction. An “effective” wind at that position for generating waves propagating toward the observation point was calculated as  $U \cos\phi^{1.63}$ , where  $U$  is the wind speed.

The term  $U \cos\phi$  is the component of the wind speed along the radial, but Walsh et al. (1989) found that wind components needed to be less effective in generating waves in slant-fetch geometries than a wind of the component magnitude blowing in that direction. In particular, the wind components needed to be degraded by raising the cosine to the 1.63 power. When  $\phi$  is small, there is little difference, but when  $\phi$  is  $55^\circ$ , the effective wind is reduced to 0.7 of the wind component along the radial.

To keep the model simple, but still acknowledge the motion of the hurricane and the travel time of the waves, an  $8.8 \text{ m s}^{-1}$  group velocity (corresponding to waves of 200 m wavelength) was used to determine how much earlier the time would have been at each position along the radial for the effect of the wind at that position to have reached the point of observation. (Group velocities for 100 m and 300 m wavelengths are  $6.2 \text{ m s}^{-1}$  and  $10.2 \text{ m s}^{-1}$ , respectively.)

The wind computation was not done in the storm-relative coordinates used elsewhere in this paper, but in an earth-relative absolute reference frame. A time offset

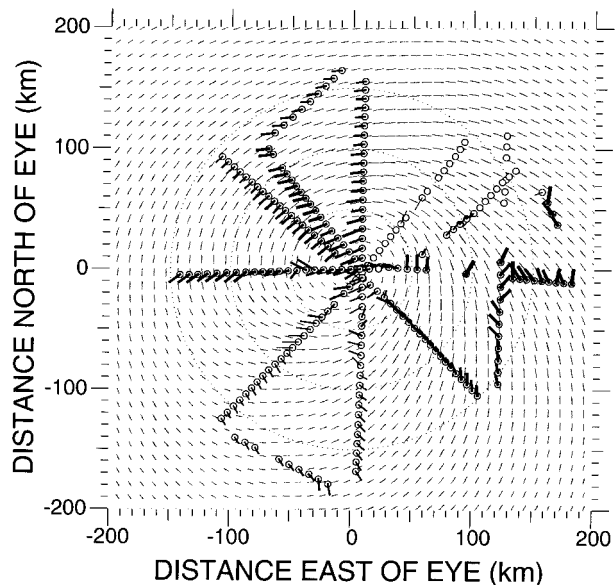


FIG. 13. Hurricane Bonnie secondary wave field in same format as Fig. 12.

determined by the distance along the radial direction and the  $8.8 \text{ m s}^{-1}$  group velocity was subtracted from the observation time of the spectrum to determine an effective time for the wind observation. The absolute location along the radial direction and the hurricane-eye position at the effective time were then used to determine the position relative to the eye for extracting the wind vector from the storm-relative HRD surface-wind field. Using an  $8.8 \text{ m s}^{-1}$  group velocity meant that the effective wind at 300 km from the observation point corresponded to the hurricane position 9.4 h earlier.

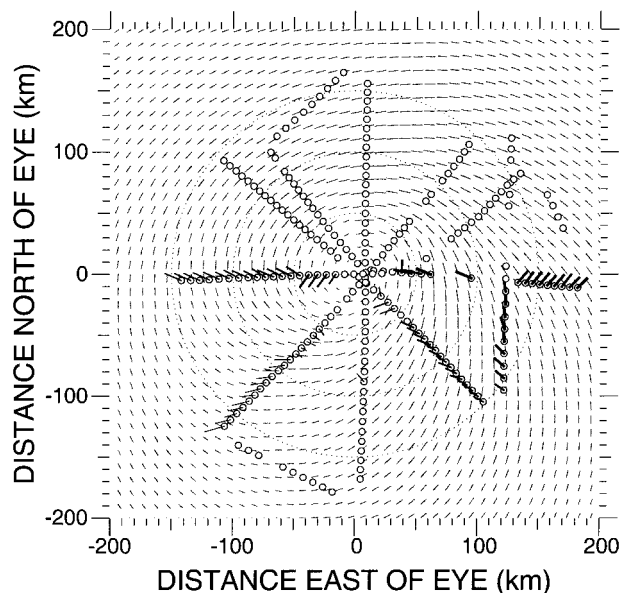


FIG. 14. Hurricane Bonnie tertiary wave field in same format as Fig. 12.

Only effective winds blowing toward the observation point were considered. Their values were squared and summed over the 300 km, following Donelan et al. (1992). This was taken to be a crude measure of the total ability of the wind along each 300 km radial direction to generate waves propagating toward the observation point.

Figure 10 shows the results of the wind computation overlaid on six spectra from various parts of Hurricane Bonnie. The sums of the squares of the effective wind values for the 36 radial directions were normalized by their peak value, multiplied by 0.07, and plotted as an indication of the cumulative relative strength of the wind field. In all six cases the maximum of the pattern agreed very well with the observed propagation direction of the dominant waves, whether they were in the wind direction (Fig. 10a), or off the wind direction by  $50^\circ$  (Figs. 10b and 10c),  $90^\circ$  (Fig. 10d),  $110^\circ$  (Fig. 10e), or even  $180^\circ$  (Fig. 10f).

All the wind-weighting patterns in Fig. 10 were fairly narrow and the spectra were relatively simple. Figure 11 shows the predictive ability of the wind-weighting pattern in a complex situation. As the aircraft traveled northward through the radius of maximum wind south of the eye, the composition of the wave field totally changed with little change in wave height (Fig. 8). The wind-weighting patterns in Fig. 11 predict the rapid change in the composition of the wave field over this 40-km interval, even though the local wind was always directed toward  $50^\circ$  and was never less than about  $25 \text{ m s}^{-1}$ .

This accomplishment is remarkable if one looks at the storm-centered wind field in Fig. 8. The wind to the southeast of the segment for the spectra of Fig. 11 is almost orthogonal to the northwest swell propagation direction evident in Fig. 11. The hurricane had been moving toward the northwest, but turned nearly due north just as the research flight entered the storm (Fig. 1), cutting across northwestward propagating waves generated at an earlier time. The simple model was able to predict the transition in the wave field because it accounted for the hurricane motion over the 10 h prior to the observations. The dashed wind-weighting pattern in Fig. 11 shows the result of holding the wind field fixed in the position it occupied at the observation time.

This simple model does not predict the dominant wavelength and is not intended to compete with even the crudest wind wave generation model. But the computation is fast enough that it can be performed at the location of every spectrum. It is of great benefit in determining which components in the encounter spectrum of a complex wave field are real.

## 5. Spatial variation of wave components

Even though the previous section showed the limitations of a storm-centered analysis of a hurricane, some cautious observations can be made in that reference

frame. For each of the three partitions in each spectrum,  $H_s$ , the wavelength, and the direction of propagation at the peak spectral density were determined and designated as primary, secondary, or tertiary wave fields based on the wave height.

Figure 12 is a plan view of the Hurricane Bonnie primary wave field. The circles indicate the data locations, and the radials extend in the wave propagation direction a length proportional to the wavelength. The width of the radials is proportional to the  $H_s$ , so the aspect ratio is an indication of wave steepness. A wide rectangle indicates steep waves, and a narrow rectangle indicates shallow waves.

The northeast quadrant of Bonnie had the most heavy rain, which resulted in data gaps caused by complete attenuation of the SRA signal. The dominance of the 300 m wavelength, 10-m high swell propagating toward the northwest is apparent. Its propagation direction is roughly aligned with the track Bonnie had for the 4-h period just prior to the observations. The northwest swell was the result of two effects. First, the wind is generally higher in the direction of motion of the hurricane because, in most cases, the forward translation of the storm adds to the wind speed in the right half of the storm (and subtracts from it on the opposite side). Second, there is a partial resonance that increases the effective fetch and duration of the wave-growth process in the direction of the motion of the storm (Shemdin 1980; Young 1988; MacAfee and Bowyer 2000a,b; Bowyer 2000). The high curvature of the wind field limits the fetch, but the waves that propagate in the direction of the motion of the storm remain under the influence of an aligned wind for a longer time and distance. This is not a new concept since the general rule that the largest waves in a hurricane are in the right forward quadrant is well known (Cline 1920; Tannehill 1936), but Fig. 12 is an impressive demonstration of it.

Also apparent in Fig. 12 is the frequent propagation of the dominant waves at a large angle to the local wind, sometimes even opposite it. Stress formulations that do not consider this phenomenon might be subject to considerable error.

Figure 13 shows a plan view of the secondary wave field. The plot should be interpreted in conjunction with the spectral shapes and the partition orientations shown in Figs. 6–9. In contrast to the primary wave field, the secondary wave field is more symmetrical spatially, and it frequently propagates near the downwind direction.

Figure 14 shows the tertiary wave field. No tertiary wave components were identifiable north of the eye because of the dominance of the northwestward propagating swell.

Figures 12, 13, and 14 indicate three directions of propagating wave fields for the northbound flight segment 120 km east of the eye: northwest, north, and northeast. At the south end of the flight segment, the northwestward propagating wave field is tertiary, but 40

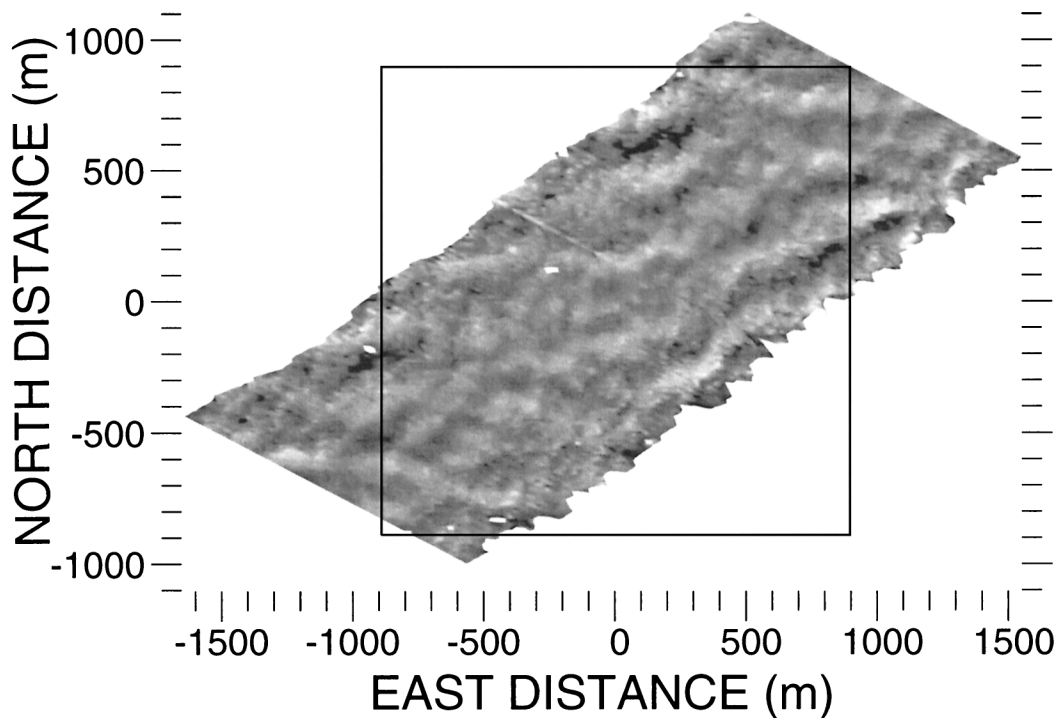


FIG. A1. Grayscale-coded topography for 180-line segment measured with the SRA when the aircraft was about 75 km north and 125 km east of the eye and traveling toward the southwest. The outline of the uniform grid the data are interpolated to is indicated by the square box.

km to the north it becomes secondary, and in another 30 km it is primary.

If only the northwest propagating wave components from Figs. 12–14 were plotted on a single figure and

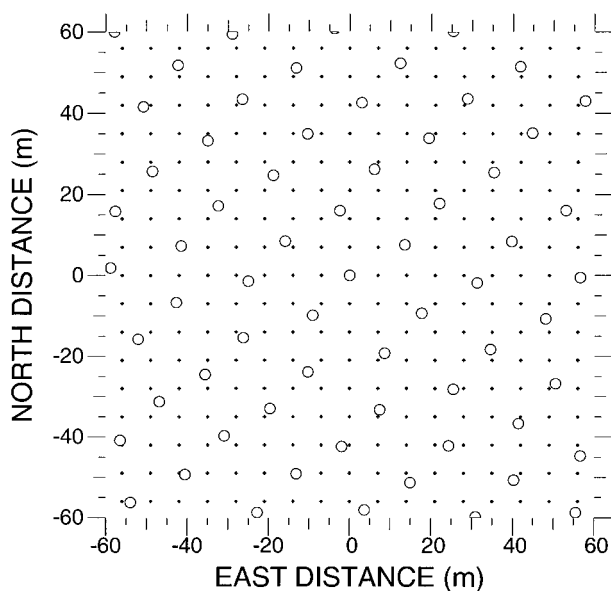


FIG. A2. Expanded region around the origin of Fig. A1. Circles indicate locations of SRA elevation measurements; dots indicate points of the uniform grid to which the data are linearly interpolated.

traced backward, they would appear to originate from a broad region in the right rear quadrant of the storm.

In 1976 there were pioneering hurricane observations with comparable coverage and resolution to that of the SRA that need to be acknowledged. They were acquired using a Jet Propulsion Laboratory synthetic aperture radar (SAR) onboard a NASA CV-990 research aircraft at 8 to 13 km altitude. Two flights were made in Hurricane Emmy, one in Hurricane Francis, and two in Hurricane Gloria. Elachi et al. (1977) and King and Shemdin (1979) essentially treated the SAR high-resolution ocean wave imagery as microwave photographs from which they could determine the direction and the wavelength of the waves. They made no attempt to use a modulation transfer function to relate the radar signature to the wave directional energy spectrum. But even without the quantitative formation of the present analysis, they were still able to point out many of the same qualitative properties of the wave field presented here.

## 6. Conclusions

The SRA has provided the first sea-surface directional wave spectrum measurements in all quadrants of the inner core of a hurricane over open water. The highest  $H_s$  in Hurricane Bonnie on 24 August 1998 was almost 11 m and individual waves up to 19 m peak to trough were observed. The highest waves and the longest wave-

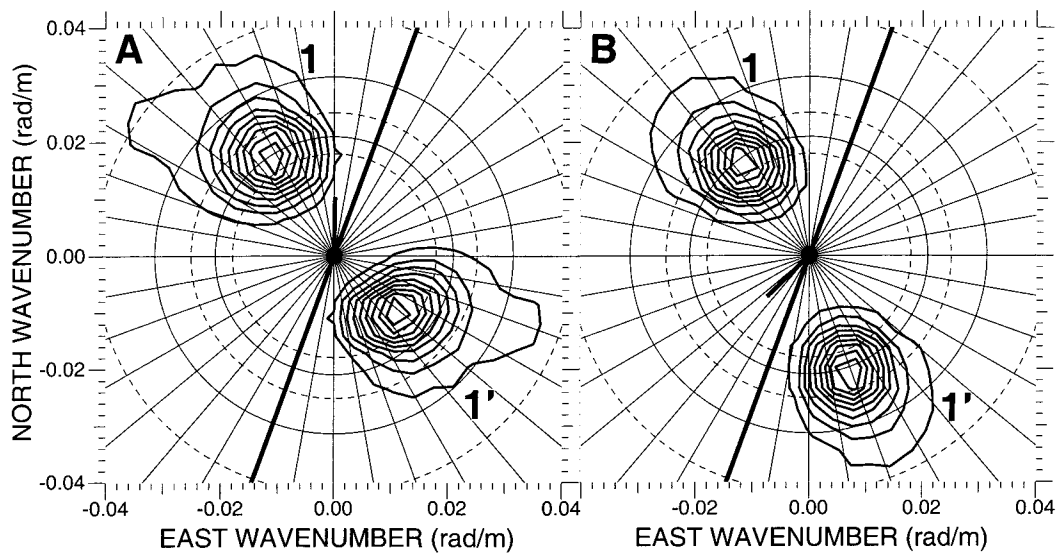


FIG. A3. Doppler-corrected spectra resulting from a northward flight line 156 km north and 10 km east of the eye (a) and a southwestward flight line about 167 km north and 9 km west of the eye (b).

lengths were observed in the right forward quadrant of the hurricane, as is commonly assumed. They are due to the typically higher wind speed resulting from the forward motion of the storm and a partial resonance between the forward motion of the storm and the group velocity of the waves propagating in that direction.

The lowest  $H_s$ , about 5.5 m, was observed in the vicinity of the radius of maximum wind in the left rear quadrant of the hurricane. A trimodal wave system existed in the right rear quadrant of Hurricane Bonnie with a total  $H_s$  of almost 8 m. Each of the three components had a dominant wavelength of about 200 m and an  $H_s$  of more than 4 m.

The dominant waves generally do not propagate in the downwind direction of the local wind, but a simple model for the effective wind-weighting pattern predicted their propagation direction, even in complex situations, when the time history of the hurricane track over the previous 10 h was considered.

An animation of the Hurricane Bonnie wave spectra can be seen online (<http://lidar.wff.nasa.gov/sra/chs2000.shtml>).

*Acknowledgments.* Donald E. Hines of EG&G Inc. maintained the SRA and Gerald S. McIntire of CSC installed it in NOAA aircraft N43RF. The authors thank the flight crew and staff of the NOAA/AOC for their help in ensuring the success of this experiment. The Science and Engineering Division deserves special recognition for work in installing the SRA on N43RF and developing the needed interfaces with the other aircraft systems. This work was supported by the NASA Solid Earth/Natural Hazards Program, the NASA Physical Oceanography Program, and the Office of Naval Research (Document N00014-98-F-0209).

## APPENDIX

### Generating and Correcting Directional Wave Spectra

Figure A1 shows a 180-line segment of grayscale-coded topography measured with the SRA when the aircraft was about 75 km north and 125 km east of Bonnie's eye and traveling toward the southwest. The SRA topographic data are processed in 180-line segments with the measured elevation points interpolated to a uniform orthogonal grid that is centered on the midpoint of the data. The axes are oriented north and east, and the outline of the uniform grid is indicated by the square box. The axes of the uniform grid each contain 256 points spaced at 7 m for a nominal spectral resolution of  $0.0035 \text{ rad m}^{-1}$ . Figure A1 demonstrates that the actual crosstrack spectral resolution is only about  $0.0052 \text{ rad m}^{-1}$ , determined by the nominal 1200-m swath width. Since the data do not fill the box, the spectral variances are multiplied by the ratio of the total area of the box to the area containing nonzero surface elevation values.

Figure A2 expands the region around the origin of Fig. A1. The circles indicate the locations of the SRA elevation measurements, and the dots indicate the points of the uniform grid to which the data are linearly interpolated. The interpolation automatically compensates for variations in ground speed and track and aircraft drift angle, which causes the SRA scan plane to deviate from the normal to the ground track.

The interpolated data are transformed by a two-dimensional FFT to obtain the directional wave spectrum in wavenumber space. The line count is advanced 100 for each new spectrum. The amount of overlap in the

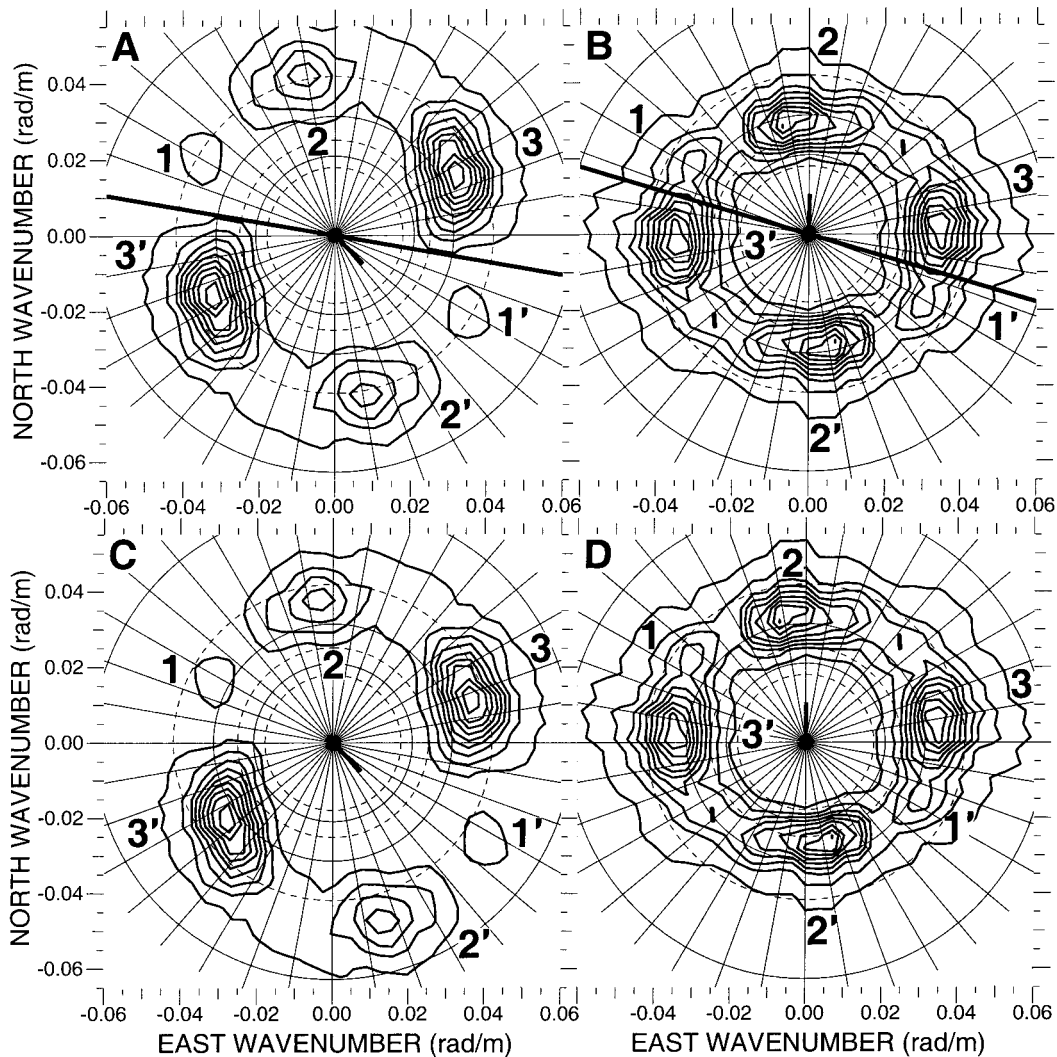


FIG. A4. Wave spectra corresponding to Fig. 6o (left side, panels a and c) and Fig. 7a (right side, panels b and d) before (top panels, a and b) and after (bottom panels, c and d) Doppler correction.

wave topography input into adjacent spectra depends on the aircraft ground track and ground speed, which varied between  $86$  and  $169 \text{ m s}^{-1}$  with a mean of  $119 \text{ m s}^{-1}$ . At the average ground speed, the overlap would be about 13%. At the lowest ground speed, the overlap would be about 40%.

Output spectra are obtained by averaging five consecutive spectra. The output spectra are additionally smoothed by using uniform weighting on a  $3 \times 3$  array of points in wavenumber space. If the input topography to the individual spectra were nonoverlapping and the uniform grid were filled, the smoothed output spectra would have 90 degrees of freedom. The actual spectra have fewer.

Each spectrum contains an ambiguity of  $180^\circ$  in the direction of propagation of the waves, which is common to all transformations from topographic maps. The FFT does not determine the actual direction of propagation

and puts half the spectral energy into the real lobe and half into an artifact lobe that is perfectly symmetric with the real lobe. The SRA processing doubles the energy everywhere in the FFT output spectrum and then deletes the energy in the half-plane containing the artifacts.

The spectra must be corrected for Doppler effects caused by ocean wave propagation. The proper Doppler corrections can be applied without any a priori information on the wave field. All wave components are corrected as if they were real. Waves propagating in the aircraft flight direction appear to be too long, and they must be shifted to higher wavenumbers (shorter wavelengths). Waves propagating opposite the aircraft flight direction appear too short, and they must be shifted to lower wavenumbers (longer wavelengths). Waves propagating at right angles to the aircraft flight track appear to have a different propagation direction. In general, corrections to both the wavelength and direction of

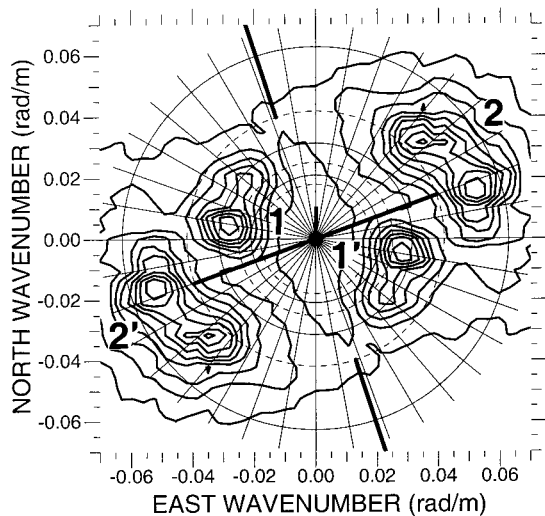


FIG. A5. Spectrum of Fig. 8e prior to Doppler correction and deletion of spectral artifact lobes ( $1'$ ,  $2'$ ).

propagation are necessary, but the net result is that all wave components are shifted only in the alongtrack direction by an amount that is proportional to the actual wavenumber magnitude (Walsh et al. 1985).

The Doppler corrections provide a way to identify the artifact lobes whenever two flight lines with significantly different headings are in proximity (Walsh et al. 1985; Wright et al. 1999). Figure A3 shows two spectra resulting from a northward flight line 156 km north and 10 km east of the eye (panel a) and a southwestward flight line about 167 km north and 9 km west of the eye (panel b). A radial of  $0.01 \text{ rad m}^{-1}$  in each panel extends from the origin in the flight direction. The spectra have been Doppler corrected, which shifts the real spectral lobes (1) from the two flight directions into their proper positions, causing their locations to coalesce. The Doppler corrections to the artifact lobes ( $1'$ ) shift them out of the symmetrical positions they occupied in the encounter spectra and cause them to separate.

The situation was very simple in Fig. A3 because there was little spatial variation in the wave field even though the centers of the two data spans were separated by 22 km. The corrected real lobes (1) both had 300 m wavelengths, and their propagation directions were both near  $325^\circ$ . The artifact-lobe wavelengths differed by more than 100 m, and their propagation directions differed by about  $30^\circ$ .

The thick diameters in Fig. A3 indicate the orientations of the half-plane boundaries used to eliminate the artifact lobes. All spectral values to the right of the boundaries were set to zero. The boundaries were not positioned orthogonal to the line joining the real and artifact lobes because the wind at this location was blowing toward  $260^\circ$  at about  $40 \text{ m s}^{-1}$  (Fig. 8k). There was a significant wind-driven sea propagating in that direction. It was not apparent in the spectrum because its

peak spectral density was less than 10% of the peak spectral density of the swell.

The left side of Fig. A4 (panels a, c) shows wave spectra corresponding to Fig. 6o and the right side (panels b, d) correspond to Fig. 7a. The numbers identify the three corresponding spectral lobes in each spectrum and the primed numbers identify the artifact lobes. The top panels (a and b) show that prior to the Doppler correction, none of the spectral components agree. After Doppler correction (bottom panels c and d) the true spectral lobes (1, 2, 3) agree much better than the artifact lobes ( $1'$ ,  $2'$ ,  $3'$ ).

The absolute agreement of the real lobes in Fig. A4 (panels c, d) is not as good as in Fig. A3 because the wave fields evolved significantly over the 20-km distance separating these two observations. But the agreement relative to the artifact lobes is still sufficient to unambiguously eliminate the artifacts.

When there is enough spatial evolution so that neither set of lobes is clearly a better match than the other, the relative positions can be used as a second-order clue. After Doppler correction, the artifact lobes are shifted from their symmetrical positions relative to the real lobes in the alongtrack direction. In panel c of Fig. A4 they are shifted toward the southeast. In panel d they are shifted toward the north. These shifts mean that the artifact lobes in panel c should be below and to the right of the artifact lobes in panel d, which they are.

The thick diameters in the top panels of Fig. A4 show the orientation of the half-plane boundary used to delete the artifact lobes, which is done prior to Doppler correction. Both of these boundaries might have been better positioned about  $5^\circ$  CW, but individual orientations were not entered into the program for each spectrum. For efficiency, half-plane orientations were identified for a subset of spectra and then linearly interpolated to the other spectra observation times.

Even though the Fig. A4 spectra have three components, they are all contained in the same half-plane. Figure A5 shows the spectrum of Fig. 8e prior to Doppler correction. No single half-plane could contain both real spectral lobes (1, 2), but having different half-plane orientations for wavelengths longer and shorter than 150 m can do a reasonable job in this instance. The 150-m wavelength boundary was arbitrarily selected after perusal of the entire dataset.

In the typical HRD hurricane inner core flight pattern over open ocean, a sequence of radials is flown through the eye, connected by segments well away from the eye. The ambiguous spectral lobes can readily be identified in the eye where the radials cross, at the corners of the flight tracks, and at any other position where flight lines cross, such as the location corresponding to Fig. 7c. With continuity, the correct spectral lobe orientations can be extrapolated throughout the flight pattern.

The half-plane boundaries were oriented subjectively, generally in regions of low spectral energy density, to keep them from distorting the spectra. When the spectral

azimuthal variation permitted, the high-wavenumber half-plane boundary was oriented nearly orthogonal to the wind direction.

## REFERENCES

- Avila, L. A., 1998: Preliminary report: Hurricane Bonnie 19–30 August 1998. NOAA National Hurricane Center/Tropical Prediction Center, 16 pp. [Available online at <http://www.nhc.noaa.gov>.]
- Bowyer, P. J., 2000: Phenomenal waves with a transitioning tropical cyclone (Luis, the Queen, and the buoys). Preprints, *24th Conf. on Hurricanes and Tropical Meteorology*, Ft. Lauderdale, FL, Amer. Meteor. Soc., 294–295.
- Cline, I. M., 1920: Relation of changes in storm tides on the coast of the Gulf of Mexico to the center and movement of hurricanes. *Mon. Wea. Rev.*, **48**, 127–146.
- Donelan, M., M. Skafel, H. Graber, P. Liu, D. Schwab, and S. Venkatesh, 1992: On the growth of wind-generated waves. *Atmos.–Ocean*, **30**, 457–478.
- Elachi, C., T. W. Thompson, and D. King, 1977: Ocean wave patterns under Hurricane Gloria: Observation with an airborne synthetic-aperture radar. *Science*, **198**, 609–610.
- Hasselmann, K., and Coauthors, 1973: Measurements of wind–wave growth and swell decay during the Joint North Sea Wave Project (JONSWAP). *Dtsch. Hydrogr. Z.*, **A8** (12) (Suppl.), 95 pp.
- King, D. B., and O. H. Shemdin, 1979: Radar observations of hurricane wave directions. *Proc. 16th Int. Conf. Coastal Eng.*, Hamburg, Germany, ASCE, 209–226.
- MacAfee, A. W., and P. J. Bowyer, 2000a: Trapped-fetch waves in a transitioning tropical cyclone (Part I—The need and the theory). Preprints, *24th Conf. on Hurricanes and Tropical Meteorology*, Ft. Lauderdale, FL, Amer. Meteor. Soc., 292–293.
- , and —, 2000b: Trapped-fetch waves in a transitioning tropical cyclone (Part II—Analytical and predictive model). Preprints, *24th Conf. on Hurricanes and Tropical Meteorology*, Ft. Lauderdale, FL, Amer. Meteor. Soc., 165–166.
- Powell, M. D., S. H. Houston, and T. A. Reinhold, 1996: Hurricane Andrew's landfall in south Florida. Part I: Standardizing measurements for documentation of surface wind fields. *Wea. Forecasting*, **11**, 304–328.
- Saffir, H. S., 1977: Design and construction requirements for hurricane resistant construction. ASCE Preprint No. 2830, American Society of Civil Engineers, New York, 20 pp.
- Shemdin, O. H., 1980: Prediction of dominant wave properties ahead of hurricanes. *Proc. 17th Int. Coastal Engineering Conf.*, Sydney, Australia, ASCE, 600–609.
- Simpson, R. H., and H. Riehl, 1981: *The Hurricane and its Impact*. Louisiana State University Press, 398 pp.
- Tannehill, I. R., 1936: Sea swells in relation to movement and intensity of tropical storms. *Mon. Wea. Rev.*, **64**, 231–238.
- Walsh, E. J., D. W. Hancock, D. E. Hines, R. N. Swift, and J. F. Scott, 1985: Directional wave spectra measured with the surface contour radar. *J. Phys. Oceanogr.*, **15**, 566–592.
- , —, —, —, and —, 1989: An observation of the directional wave spectrum evolution from shoreline to fully developed. *J. Phys. Oceanogr.*, **19**, 670–690.
- , L. K. Shay, H. C. Graber, A. Guillaume, D. Vandemark, D. E. Hines, R. N. Swift, and J. F. Scott, 1996: Observations of surface wave–current interaction during SWADE. *Global Atmos. Ocean Syst.*, **5**, 99–124.
- Wright, C. W., E. J. Walsh, D. Vandemark, W. B. Krabill, and A. Garcia, 1999: Hurricane directional wave spectrum measurement with a scanning radar altimeter. *Proceedings of the Third International Workshop on Very Large Floating Structures (VLFS'99)*, R. C. Ertekin and W. J. Kim, Eds., Vol. 1, U.S. Office of Naval Research, 37–41.
- Young, I. R., 1988: Parametric hurricane wave prediction model. *J. Waterway, Port, Coastal Ocean Eng.*, **114**, 637–652.